PHYSICAL REVIEW B **109**, L121403 (2024)

Letter

Second-order topological states in a sixfold symmetric quasicrystal

Yuzhong Hu, Songmin Liu, Baoru Pan, Pan Zhou ,[*] and Lizhong Sun [†]
Hunan Provincial Key laboratory of Thin Film Materials and Devices, School of Materials Science and Engineering, Xiangtan University, Xiangtan 411105, China

(Received 20 December 2023; revised 23 February 2024; accepted 28 February 2024; published 13 March 2024)

Recently, higher-order topology has been expanded to encompass aperiodic quasicrystals, including those with eightfold or twelvefold rotational symmetry. The underlying mechanism for these high-order topological phases is generally protected by $C_n\mathcal{M}_z$ symmetry, resulting in the presence of n corner states. However, this mechanism is not applicable to other C_{2N} quasicrystals when N is an odd number. In this work, we propose the realization of a second-order topological superconductor (SOTSC) within a sixfold symmetric bronze-mean hexagonal quasicrystal with six Majorana zero-energy modes. This SOTSC emerges from the combination of vertical and horizontal mirror symmetries, which flips the mass-term sign along the horizontal mirror-invariant line and produces Majorana zero-energy modes at each corner of the quasicrystal sample. Moreover, this mechanism can extend to quasicrystals with C_{4N+2} and C_{4N} rotational symmetries, namely encompassing systems with C_{2N} symmetry. Our findings provide useful guidance for achieving SOTSC in quasicrystals featuring C_{2N} rotational symmetry and introduce bronze-mean hexagonal quasicrystals as a promising platform for exploring quasicrystal SOTSC.

DOI: 10.1103/PhysRevB.109.L121403

Introduction. There has been a significant surge in research interest regarding higher-order topological insulators/superconductors (HOTIs/HOTSCs) [1–66], which extends beyond the scope of conventional (first-order) topological phases [67,68]. HOTIs/HOTSCs, existing in d dimensions, exhibit gapless boundary states in $d-n$ dimensions ($n \geqq 2$). For instance, a second-order topological insulator/superconductor (SOTI/SOTSC) in two dimensions (2D) manifests 0D corner/Majorana states localized at its corners. Until now, HOTIs/HOTSCs has been extensively studied on crystalline systems. Recently, a lot of attention has been directed toward aperiodic systems, particularly quasicrystals, as intriguing platforms for realizing higher-order topological states [69–83]. Quasicrystalline systems featuring forbidden rotational symmetries, such as C_5, C_8, and C_{12}, serve as a promising platform for exploring novel topological phases that expand the current topological classification of crystalline materials.

However, in quasicrystals with C_8 (or C_{12}) symmetries, the corner states are generally protected by the combined symmetry $C_{8(12)}\mathcal{M}_z$, which make the mass-term sign alternate at the corners of the 0D systems, leading to the emergence of corner states. The number of them is equal to the order of rotational symmetry [see Fig. 1(a) for C_8 quasicrystal]. This mechanism to induce higher-order topological states can be applied to quasicrystals with C_{4N} rotational symmetry (N is a positive integer) but not to that with C_{4N+2} rotational symmetry. The typical example with $N = 1$ (C_6) is shown in Fig. 1(b). The corner states can not emerge at the two horizonal corners due to the identical signs at adjacent edges. Therefore, it raises the question of whether there are alternative mechanisms to induce six ($4N + 2$) corner modes in C_6 (or more general C_{4N+2}) symmetric quasicrystal. Moreover, it is of great interest to explore the new mechanism of higher-order topological phases in crystal with C_6 symmetry.

In this work, we propose bronze hexagonal quasicrystals exhibiting C_6 symmetry that can function as a platform for achieving 2D SOTSC. The emergence of this quasicrystal SOTSC stems from the combined symmetry of vertical and horizontal mirrors, which results in a reversal of the mass-term sign on either side of the horizontal mirror-invariant line, giving rise to Majorana zero-energy modes at each corner of the quasicrystal sample. These Majorana zero-energy modes exhibit resilience against symmetry-preserving perturbations, provided that both the bulk and edges maintain their gap. Additionally, this mechanism is extendable to quasicrystals featuring C_{4N+2} and C_{4N} rotational symmetries, essentially applying to quasicrystalline systems with C_{2N} symmetry.

Results and discussion. One notable example of quasicrystal lattices possessing C_6 rotational symmetry is the bronze-mean hexagonal quasicrystal [87], as illustrated in Figs. 2(a) and 2(b). The unique symmetrical and aperiodic characteristics of the hexagonal quasicrystal can be attributed to the existence of an irrational ratio between two length scales that determine its structural arrangement. The bronze-mean tiling consists of three types of tiles, each associated with two different lengths: small equilateral triangles with an edge length denoted by s, large equilateral triangles with an edge length indicated as e, and rectangles with dimensions of $s \times e$. The procedure for generating hexagonal quasicrystals using the inflation method is shown in Fig. S1 [88].

---

[*] zhoupan71234@xtu.edu.cn
[†] lzsun@xtu.edu.cn

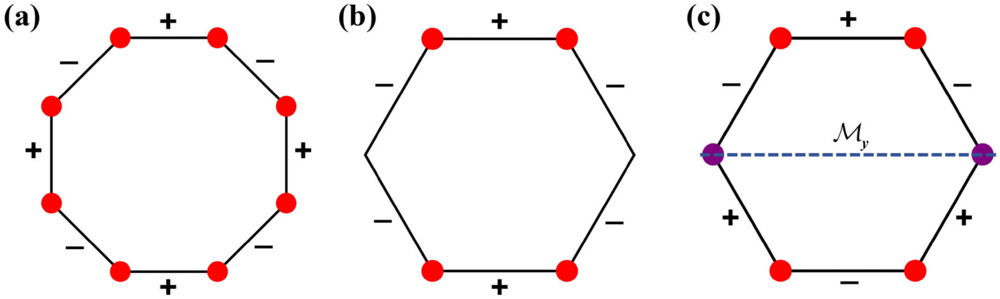

FIG. 1. The arrangement of edge mass terms and domain wall states along the perimeter of (a) eightfold and (b) sixfold symmetric quasicrystal samples. In the case of the latter, domain wall states will not form on the two corners of the $\mathcal{M}_y$-invariant line, as the adjacent boundaries of these corners have the same signs of mass terms. (c) However, if a Wilson mass term with alternating sign is introduced, six corner states can be formed in the sixfold symmetric quasicrystal.

Our investigation begins with the analysis of a 2D topological superconductor (TSC) model on this lattice, as outlined in the methods section of the Appendix. This particular model describes a system featuring 2D first-order TSCs with opposite Chern numbers within class D [69,89,90] (with parameters $t = \Delta = 1$ and $\mu = -1.5$), representing fermions subject to p-wave odd momentum pairing, denoted as $\Delta(\mathbf{p}) = -\Delta(-\mathbf{p})$. The system displays counterpropagating Majorana edge modes along its boundary, as illustrated in Figs. 2(c) and 2(d). The real-space Bogoliubov-de-Gennes (BdG) Hamiltonian $\mathcal{H}$ for this system has particle-hole symmetry ($\mathcal{P}$), satisfied by the relation $\{\mathcal{H}, \mathcal{P}\} = 0$, with $\mathcal{P}$ representing an antiunitary operator given by $\mathcal{P} = \tau_z\sigma_x\mathbb{1}\mathcal{K}$, where $\mathcal{K}$ denotes complex conjugation, and $\mathbb{1}$ signifies the identity operator within the quasicrystal lattice site space. Additionally, the system exhibits three mirror symmetries denoted as $\mathcal{M}_i$ ($i = x, y, z$), which satisfy the commutation relation $[\mathcal{H}, \mathcal{M}_i] = 0$, with $\mathcal{M}_x = i\tau_x\sigma_x\mathcal{R}_x$, $\mathcal{M}_y = i\tau_x\sigma_y\mathcal{R}_y$, and $\mathcal{M}_z = \tau_z\sigma_0\mathbb{1}$. Here, $\mathcal{R}_{x,y}$ are orthogonal matrices that flip the entire system vertically and horizontally by permuting the sites of the tiling. The mirror symmetry $\mathcal{M}_z$ endow the system with a $\mathbb{Z}_2$ topological structure, determined by the parity of

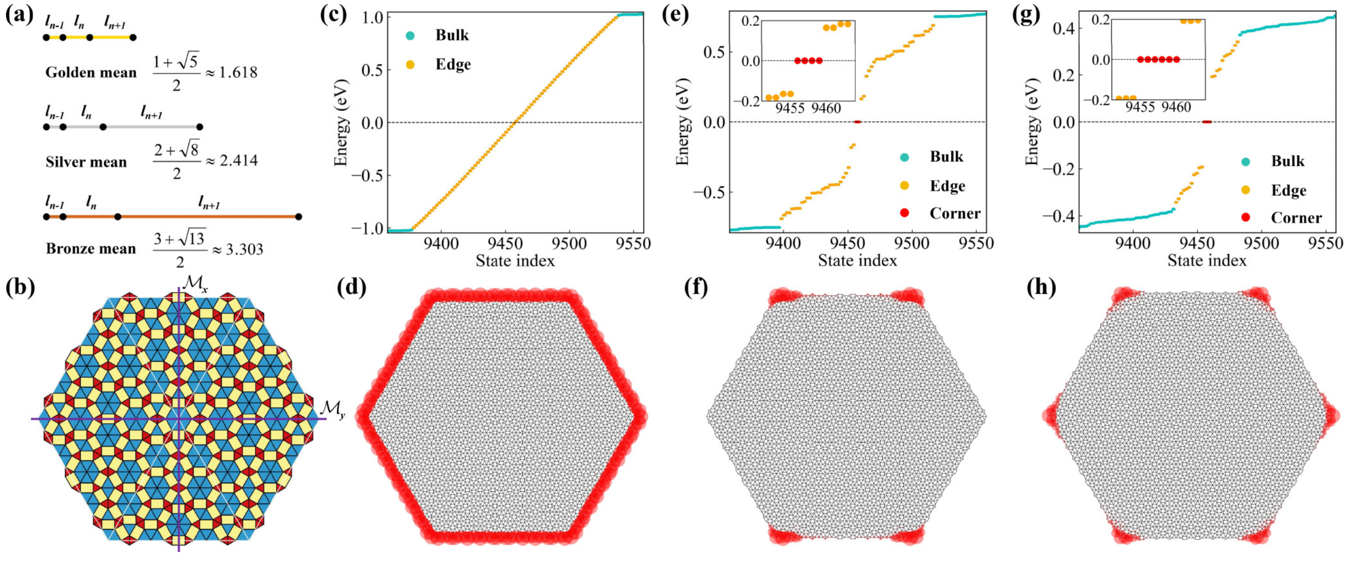

FIG. 2. (a) The metallic means [84] is hidden in the geometry of quasicrystals. The side of the primitive tile of quasicrystals l in the nth generation denoted by l_n is determined by the recurrence relation $l_{n+1} = k \cdot l_n + l_{n-1}$. The inflation factor is defined by $\frac{l_{n+1}}{l_n} = \frac{k+\sqrt{k^2+4}}{2}$ and referred to as the metallic means. When $k = 1, 2, 3$ corresponds to gold related to Penrose tiling [85], silver related to AB tiling [86], and bronze mean [87], respectively. (b) The hexagonal quasicrystal [87] with bronze mean $\frac{3+\sqrt{13}}{2}$ is composed of three types of primitive tile based on two lengths: small colored in red and large colored in blue equilateral triangles, and rectangles colored in yellow with the ideal length ratio $\frac{e}{s} = \frac{\sqrt{3}+\sqrt{39}}{6}$. (c) Energy spectrum of the first-order TSCs BdG Hamiltonian on a hexagonal quasicrystal vs the eigenvalue index. The orange dots mark all the Majorana edge modes. (d) The probability density of doubly degenerate eigenstates is marked by the orange dot in (c). (e), (g) The energy spectrum of the HOTSCs Hamiltonian versus the eigenvalue index for the mass term $\mathcal{V}^{x0}$ and $\mathcal{V}^{xx}$, respectively. (f), (h) The probability density of zero-energy modes in (e) and (g), respectively. The color map shows the values of the probability density. We take the model parameters $\Delta = 1$, $t = 1$, $\mu = -1.5$, $V = 1$, and lattice site number $N = 4729$. For the first-order TSCs, the system hosts counterpropagating Majorana modes on any edge, protected by mirror symmetry. For mass term, $\mathcal{V}^{x0}$ or $\mathcal{V}^{xx}$ gaps out the edge, leading to the higher-order topological phase.

TABLE I. Symmetries of the BdG Hamiltonian $\mathcal{H}$ on the bronze mean tiling quasicrystalline lattice with the hexagonal boundaries without and with mass term $\mathcal{V}$. $\sigma_{x,y,z}$ and $\tau_{x,y,z}$ are the Pauli matrices. $\mathcal{K}$ is the complex conjugate operator, and $\mathbb{1}$ is the $N \times N$ unit matrix with the lattice number N. $\mathcal{R}_{x,y}$, are orthogonal matrices permuting the sites of the tiling to flip the whole system vertically and horizontally. $\mathcal{R}_{2,6}$ are orthogonal matrix permuting the sites of the tiling to rotate the whole system by an angle of π and $\frac{\pi}{3}$, respectively. Check marks indicate that the symmetry in this case is preserved, and a cross mark means the symmetry is absent.

		$\mathcal{V}=0$	$\mathcal{V}=\mathcal{V}^{x0}$	$\mathcal{V}=\mathcal{V}^{xx}$	$\mathcal{V}=\mathcal{V}^{xy}$
$\mathcal{P}=\sigma_z\tau_x\mathbb{1}\mathcal{K}$	$\mathcal{P}\mathcal{H}\mathcal{P}^{-1}=-\mathcal{H}$	✓	✓	✓	✓
$C_6=\exp(-i\frac{\pi}{6}\sigma_0\tau_z)\mathcal{R}_6$	$C_6\mathcal{H}C_6^{-1}=\mathcal{H}$	✓	×	×	×
$C_2=i\sigma_0\tau_z\mathcal{R}_2$	$C_2\mathcal{H}C_2^{-1}=\mathcal{H}$	✓	✓	×	×
$\mathcal{M}_x=i\sigma_x\tau_x\mathcal{R}_x$	$\mathcal{M}_x\mathcal{H}\mathcal{M}_x^{-1}=\mathcal{H}$	✓	✓	✓	×
$\mathcal{M}_y=i\sigma_x\tau_y\mathcal{R}_y$	$\mathcal{M}_y\mathcal{H}\mathcal{M}_y^{-1}=\mathcal{H}$	✓	✓	×	✓
$\mathcal{M}_z=\sigma_z\tau_0\mathbb{1}$	$\mathcal{M}_z\mathcal{H}\mathcal{M}_z^{-1}=\mathcal{H}$	✓	×	×	×
$C_6\mathcal{M}_x$	$C_6\mathcal{M}_x\mathcal{H}(C_6\mathcal{M}_x)^{-1}=\mathcal{H}$	✓	×	×	×
$C_6\mathcal{M}_y$	$C_6\mathcal{M}_y\mathcal{H}(C_6\mathcal{M}_y)^{-1}=\mathcal{H}$	✓	×	×	×
$C_6\mathcal{M}_z$	$C_6\mathcal{M}_z\mathcal{H}(C_6\mathcal{M}_z)^{-1}=\mathcal{H}$	✓	×	×	×
$C_2\mathcal{M}_z$	$C_2\mathcal{M}_z\mathcal{H}(C_2\mathcal{M}_z)^{-1}=\mathcal{H}$	✓	×	✓	✓
$\mathcal{M}_x\mathcal{M}_z$	$\mathcal{M}_x\mathcal{M}_z\mathcal{H}(\mathcal{M}_x\mathcal{M}_z)^{-1}=\mathcal{H}$	✓	×	×	✓
$\mathcal{M}_y\mathcal{M}_z$	$\mathcal{M}_y\mathcal{M}_z\mathcal{H}(\mathcal{M}_y\mathcal{M}_z)^{-1}=\mathcal{H}$	✓	×	✓	×

the number of helical Majorana edge modes [48]. Moreover, owing to the distinctive shape of the tiling, the system possesses a global sixfold rotation symmetry centered around its core, given by $[\mathcal{H}, C_6]=0$, where $C_6=\exp(-i\frac{\pi}{6}\sigma_0\tau_z)\mathcal{R}_6$. Here, $\mathcal{R}_6$ is an orthogonal matrix responsible for rotating the entire system by an angle of $\frac{\pi}{3}$ by permuting the lattice sites. For a more comprehensive understanding of the symmetry analysis associated with the BdG Hamiltonian $\mathcal{H}$, additional details can be found in Table I.

In order to produce the SOTSC phase, a mass term is incorporated into the BdG Hamiltonian $\mathcal{H}$ through inclusion of the following term:

$$\mathcal{V}^{pq}=\frac{V}{2}\sum_{\langle j,k\rangle}\Psi_j^\dagger[\mathrm{sgn}(j-k)\sigma_p\tau_q\cos(3\alpha_{jk})]\Psi_k, \tag{1}$$

where σ_p or τ_q (p or q can take the values 0, x, y, and z) represent the 2×2 identity matrix and the three components of the Pauli matrices, respectively. The α_{jk} is the angle between the bonding direction and the horizontal direction [70], V represents the amplitude of the mass term, and $\mathrm{sgn}(j-k)$ means if $j-k\ >0$ return $+1$ or $j-k\ <0$ return -1. The mass term $\mathcal{V}^{pq}$ has sixteen possible terms in total, but only four of them ($\mathcal{V}^{x0}$, $\mathcal{V}^{xx}$, $\mathcal{V}^{y0}$, and $\mathcal{V}^{yx}$) are capable to gap out the Majorana edge modes and consequently give rise to Majorana zero-energy corner modes. In the subsequent discussion, since $\mathcal{V}^{x0}$ and $\mathcal{V}^{xx}$ yield the same results as $\mathcal{V}^{y0}$ and $\mathcal{V}^{yx}$, respectively, our focus will be exclusively on the two specific terms $\mathcal{V}^{x0}$ and $\mathcal{V}^{xx}$. The remaining terms are addressed in Sec. II of the Supplemental Material [88].

The results obtained by incorporating $\mathcal{V}^{x0}$ are depicted in Figs. 2(e) and 2(f). It is observed that the gapless Majorana edge states become gapped, and four Majorana zero-energy modes emerge within this gap around the Fermi level, primarily localized at the four corners of the upper and lower edges. The opening of the gap can be explained by the anticommutative relationship of $\{\mathcal{V}^{x0}, \mathcal{M}_z\}=0$. These nontrivial Majorana zero-energy modes can be explained through the Jackiw-Rebbi mechanism [91]. According to this mechanism, Majorana zero-energy modes emerge when a domain wall with varying mass is present. If the gapless Majorana edge modes are gapped, the edge Hamiltonian can be described by a 1D Dirac model with a mass term denoted as

$$\mathcal{H}_{\mathrm{edge}}=-iv(l)\partial_l\sigma_z+m(l)\sigma_x, \tag{2}$$

where l represents the real-space coordinate along the boundary of sixfold symmetric quasicrystals. As a rough approximation, however, we can view an edge of the hexagonal sample boundary as an extended "bond." The sign of the effective Wilson mass for the Majorana edge mode is determined by the orientation of the edge, represented by the polar angle α_{jk}, and the Kronecker product of spin and electron-hole degrees of freedom, denoted as $\sigma_p\tau_q$. Indeed, this effective edge Hamiltonian can be obtained from an effective $k\cdot p$ Hamiltonian expanded around Γ under the long-wavelength approximation [79].

The factor $\cos(3\alpha_{jk})$ determines the initial distribution of the mass-term sign in the sample, as shown in Fig. 1(b). By considering the $\sigma_x\tau_0$, the $\mathcal{V}^{x0}$ adheres to the $\mathcal{M}_x$ and $\mathcal{M}_y$ symmetries (detailed in Table I). In contrast to the eightfold quasicrystal with $C_8\mathcal{M}_z$ symmetry [69,70], the preservation of $\mathcal{M}_x$, $\mathcal{M}_y$ symmetries in the hexagonal quasicrystal where $\mathcal{V}^{x0}$ is introduced prevents the sign of the mass term to alternate along the sample boundary. This indicates that the mass term $\mathcal{V}^{x0}$ shares the same sign of $\cos(3\alpha_{jk})$. As depicted in Fig. 2(f), four Majorana zero-energy modes emerge at the adjoining boundaries of the upper and lower corners within the sample, attributed to opposing mass-term signs. However, Majorana zero-energy modes do not manifest at the two corners along the $\mathcal{M}_y$-invariant line, as their adjacent boundaries feature identical mass-term signs.

Now, let's delve into the scenario involving the mass term $\mathcal{V}^{xx}$, which breaks the C_6 and two mirror ($\mathcal{M}_y$ and $\mathcal{M}_z$) symmetries, while it preserves the $\mathcal{M}_y\mathcal{M}_z$ symmetry. Importantly, the symmetries $\mathcal{M}_y$ and $\mathcal{M}_z$ anticommute with the mass term $\mathcal{V}^{xx}$, namely $\{\mathcal{V}^{xx}, \mathcal{M}_y\}=0$ and $\{\mathcal{V}^{xx}, \mathcal{M}_z\}=0$, leading to the opening of a band gap in the Majorana edge modes. Meanwhile, the $\mathcal{M}_y\mathcal{M}_z$ symmetry induces an initial distribution of mass-term sign flips between $\mathcal{M}_y$-contrasting edges, as illustrated in Fig. 1(c). The signs of the mass terms at the

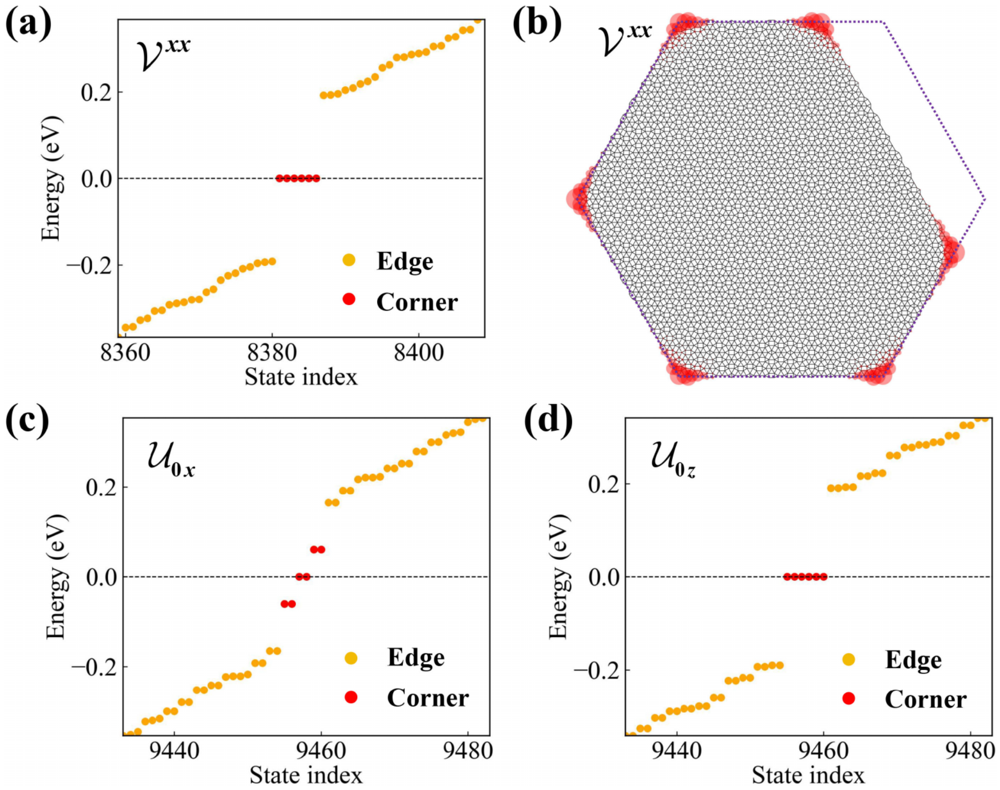

FIG. 3. (a) Energy spectrum of the Hamiltonian $\mathcal{H}$ in finite asymmetric sample vs the eigenvalue index for the mass term $\mathcal{V}^{xx}$. (b) The probability density of eigenstates marked by the red dot in (a). For the symmetric sample with lattice number $N = 4192$, we take the parameters $\Delta = 1$, $t = 1$, $\mu = -1.5$, and $V = 1$. (c), (d) The spectrum of Hamiltonian $\mathcal{H}$ with perturbation $\mathcal{U}_{0x}$ and $\mathcal{U}_{0z}$ vs the eigenvalue index in the symmetric sample with $\mathcal{V}^{xx}$, respectively. We take the parameters $\Delta = 1$, $t = 1$, $\mu = -1.5$, $V = 1$, the on-site potential strength $U = 0.1$, and the lattice number $N = 4729$.

adjacent boundaries of the two corners along the $\mathcal{M}_y$-invariant line change from being the same to being opposite. In other words, the sign of the mass term alternates between adjacent boundaries encircling the perimeter of the sample, leading to six Majorana zero-energy modes localized at each corner of the hexagonal tiling, as shown in Fig. 2(h).

The inherent quasiperiodicity of a quasicrystal implies that any finite region within an infinite sample recurs. Consequently, there are numerous locations within the quasicrystal closely resembling the vicinity of a corner in an exactly symmetric sample with $\mathcal{M}_y\mathcal{M}_z$ symmetry. To investigate the robustness of the higher-order topological phases with these local symmetries and breaking of the global $\mathcal{M}_y\mathcal{M}_z$ symmetry, we further calculate the Majorana zero-energy modes from asymmetric cutouts of the quasicrystal system with mass term $\mathcal{V}^{xx}$. As depicted in Figs. 3(a) and 3(b), we observe the emergence of six Majorana zero-energy modes in an asymmetric sample, which indicates the robustness of the zero-energy mode under the broken global $\mathcal{M}_y\mathcal{M}_z$ symmetry.

To further verify the topological origin of Majorana zero-energy modes, we investigate the robustness of these modes to various on-site potential perturbations that break symmetries. In our subsequent calculations, we denote the perturbations as

$$\mathcal{U}_{pq} = U\sum_j \Psi_j^\dagger \sigma_p \tau_q \Psi_j, \qquad (3)$$

where U represents the strength of the on-site potential. There are 16 potential on-site perturbation terms, denoted as $\mathcal{U}_{pq}$. In the main text, we present the results of two types of perturbations, namely $\mathcal{U}_{0x}$ and $\mathcal{U}_{0z}$ (for more information about other perturbations, please refer to Sec. IV of the Supplemental Material [88]). As shown in Figs. 3(c) and 3(d), when we add perturbation terms to the quasicrystalline Hamiltonian $\mathcal{H}$ (including the mass term $\mathcal{V}^{xx}$), we observe that the gapless Majorana zero-energy modes are eliminated by the perturbation $\mathcal{U}_{0x}$, while the Majorana zero-energy mode remains unaffected by the perturbation term $\mathcal{U}_{0z}$. Through symmetry analysis (detailed in Table S1 [88]), we discover that the perturbation $\mathcal{U}_{0x}$ breaks the symmetries $\mathcal{M}_y\mathcal{M}_z$, $C_2\mathcal{M}_z$, and $\mathcal{P}$, whereas $\mathcal{U}_{0z}$ only breaks the combined symmetry $\mathcal{M}_y\mathcal{M}_z$. The results indicate that as long as the system with mass term $\mathcal{V}^{xx}$ maintains the combined symmetry constraints of $C_2\mathcal{M}_z$ and/or $\mathcal{M}_y\mathcal{M}_z$, the gapless Majorana zero-energy modes are robust to weak perturbations. In other words, the Majorana zero-energy modes that appear after the symmetry $\mathcal{M}_y\mathcal{M}_z$ flips the sign of the mass term are protected by $C_2\mathcal{M}_z$ symmetry.

Here, we turn to explore the topological invariants of higher-order topological states in sixfold quasicrystals. The topological invariants of quasicrystals are generally obtained from the eigenstates of compound operation $C_n\mathcal{M}_z$ [69,70,81]. However, the mass terms in our model break the $C_6\mathcal{M}_z$ symmetry. Here we employ the eigenstates of

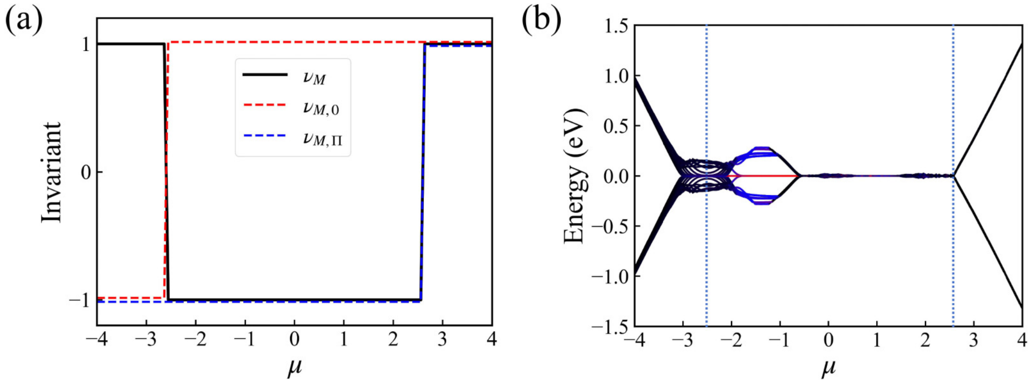

FIG. 4. The energy spectrum as a function of chemical potential μ with $t = \Delta = V = 1$, and and lattice site number $N = 4729$. (a) Topological invariants $\nu_{M,0}$, $\nu_{M,\Pi}$, and $\nu_M = \nu_{M,0}\nu_{M,\Pi}$. The topological phase transitions occur near $\mu \approx \pm 2.6$. (a) Spectrum of the 30 states closest to zero energy in a finite sample. The line color shows the weight of the state on the corners (red), edges (blue), and bulk (black). The bulk gap closes at certain μ without affecting the topological properties.

compound operation $\mathcal{M}_y\mathcal{M}_z$ because it commutes with the Hamiltonian [92]. Since $(\mathcal{M}_y\mathcal{M}_z)^2 = +\mathbb{1}$, the eigenvalues of it can be $+1$ or -1, and their eigenstates are linked by the particle-hole symmetry $\mathcal{P}$. Subsequently, a $\mathbb{Z}_2$ invariant ν_M in the two reflection sectors is defined as

$$\nu_M = \text{sign}[\text{pf}\mathcal{H}_\pm(\mathbf{k}_0) \cdot \text{pf}\mathcal{H}_\pm(\mathbf{k}_\pi)], \tag{4}$$

where pf denotes the Pfaffian, and $\mathbf{k}_0 = (0, \cdots, 0)$ and $\mathbf{k}_\pi = (\pi, \cdots, \pi)$ represent high-symmetry momentum. $\mathcal{H}_\pm$ is the Hamiltonian restricted to the ± 1 eigensubspace of $\mathcal{M}_y\mathcal{M}_z$. The selection of the reflection sector is arbitrary ($\mathcal{H}_+$ or $\mathcal{H}_-$) since they can yield identical topological invariants. Consequently, a robust $\mathbb{Z}_2$ invariant is established as $\nu_M = \nu_{M,0}\nu_{M,\Pi}$. By conducting numerical computations, we observe a band inversion occurring at $\mu \approx \pm 2.6$, with the topological invariant $\nu_M = -1$ existing between these thresholds, as depicted in Fig. 4(a). The eigenvalues corresponding to different μ values in Fig. 4(b) demonstrate that the Hamiltonian supporting nontrivial invariants exhibit nontrivial Majorana zero-energy corner modes.

Additionally, the mechanism that achieves higher-order topology in sixfold quasicrystal is also applicable to other quasicrystal systems with C_{4N+2} rotational symmetries (see Sect. V of the Supplemental Material [88] for details). For example, we have achieved higher-order topology in tenfold quasicrystal by the combined symmetry $\mathcal{M}_y\mathcal{M}_z$ when the mass term $\mathcal{V}^{xx}$ is introduced, as shown in Fig. S5 [88]. The symmetry $\mathcal{M}_y\mathcal{M}_z$ flips the initial distribution of the mass-term sign with respect to the $\mathcal{M}_y$-invariant line, so that the sign of the mass term alternates between adjacent boundaries encircling the perimeter of the sample, leading to ten Majorana zero-energy modes. Moreover, by substituting the factor in the mass term from $\cos(\frac{4N}{2}\alpha_{jk})$ to $\sin(\frac{4N}{2}\alpha_{jk})$, our mechanism extends its applicability to quasicrystalline systems possessing C_{4N} symmetry (see Sec. V of the Supplemental Material [88]). Within quasicrystals featuring C_{4N} symmetry, the mass term $\mathcal{V}^{x0}$ concurrently anticommutes with $\mathcal{M}_x$, $\mathcal{M}_y$, and $\mathcal{M}_z$ symmetries, leading to the formation of a band gap in the Majorana edge modes. Simultaneously, the joint influence of symmetries $\mathcal{M}_x\mathcal{M}_z$ and $\mathcal{M}_y\mathcal{M}_z$ results in the mass-term sign alternating along the sample boundaries, thereby generating Majorana zero-energy modes at each corner of the sample, as shown in Figs. S7 and S8 [88]. This suggests that our mechanism applies to quasicrystalline systems with C_{2N} symmetry, encompassing both C_{4N+2} and C_{4N}.

Recently, the higher-order topological phase of 2D quasicrystals has been extended to higher-order topological semimetals in 3D quasicrystals [83,93]. Similarly, a fascinating 3D higher-order topological semimetal can also be realized in sixfold symmetric quasicrystals. Here, we assume the quasicrystal is periodic along the z axis and the interlayer Hamiltonian $\mathcal{H}_{\text{inter}}$ can be expressed as follows:

$$\mathcal{H}_{\text{inter}} = t_z \cos(k_z) \sum_j \Psi_j^\dagger \sigma_x \tau_x \Psi_j, \tag{5}$$

where t_z represents the magnitude of the interlayer interaction. After introducing this Hamiltonian, it is found that the Hamiltonian is topologically nontrivial for $-0.5\pi \leqslant k_z \leqslant 0.5\pi$ and trivial for other values of k_z. The results of our numerical calculations are presented in Fig. S9 [88], revealing that the hinge states are clearly visible near the Fermi level within the range of $-0.5\pi \leqslant k_z \leqslant 0.5\pi$, and there are no hinge states in other ranges of k_z.

Conclusion. To sum up, we propose that a 2D quasicrystalline SOTSC with six corner states can be realized on a bronze hexagonal quasicrystal. The realization of such a quasicrystalline SOTSC is based on the combined symmetry of vertical and horizontal mirrors, which causes a sign change in the mass term with respect to the horizontal mirror. Furthermore, our calculations demonstrate that the nontrivial corner states remain robust even under global symmetry breaking and weak perturbations. This mechanism is also applicable to quasicrystals with rotational symmetries of C_{4N+2} and C_{4N}, indicating its broad applicability in quasicrystalline systems with C_{2N} symmetry. Recently, the HOTIs has been realized in artificial systems like photonic [38] or acoustic [30] metamaterials, ultracold atoms [94], and even topolectrical circuits [74]. Similarly, we can realize the sixfold symmetric higher-order topological states with specific structure and "hopping" interactions. Consequently, we anticipate that our proposal will swiftly capture theoretical interest in noncrystalline systems and may promptly attract experimental attention.

Acknowledgments. This work is supported by the Excellent Youth Funding of Hunan Provincial Education Department (22B0175), Natural Science Foundation of Hunan Province (No. 2023JJ30572), the Scientific Research Fund of Hunan Provincial Education Department (18A051), the National Natural Science Foundation of China (Grants No. 11804287, No. 11574260, and No. 12204397).

Appendix: Methods. We consider a model describing a 2D TSC within class D [69,89,90], representing fermions subject to p-wave odd momentum pairing, denoted as $\Delta(\mathbf{p}) = -\Delta(-\mathbf{p})$. To construct the real-space Bogoliubov-de-Gennes (BdG) Hamiltonian, we associate sites and hoppings to the vertices and edges of a C_n symmetric quasicrystal lattice. The BdG Hamiltonian is expressed in the following form:

$$\mathcal{H} = \sum_{j} \Psi_j^{\dagger} \mathcal{H}_j \Psi_j + \sum_{\langle j,k \rangle} \Psi_j^{\dagger} \mathcal{H}_{jk} \Psi_k, \tag{A1}$$

with $\Psi_j^{\dagger} = (\psi_{j,\uparrow}^{\dagger}, \psi_{j,\uparrow}, \psi_{j,\downarrow}^{\dagger}, \psi_{j,\downarrow})$, where $\psi_{j,\sigma}^{\dagger}$ represents the fermionic creation operator for a particle on site j with spin σ, and $\langle \cdots \rangle$ indicates sites connected by a bond. The on-site Hamiltonian is

$$\mathcal{H}_j = \mu \sigma_z \tau_z, \tag{A2}$$

where μ signifies the chemical potential. Pauli matrices $\boldsymbol{\tau}$ and $\boldsymbol{\sigma}$ operate on the electron-hole and spin degrees of freedom, respectively. The hopping terms takes the form:

$$\mathcal{H}_{jk} = \frac{t}{2} \sigma_z \tau_z + \frac{\Delta}{2i} [\cos(\alpha_{jk}) \sigma_z \tau_x + \sin(\alpha_{jk}) \sigma_z \tau_y], \tag{A3}$$

with t representing the normal hopping strength, Δ denoting the p-wave pairing strength [95–98], and α_{jk} indicating the angle formed by the hopping with respect to the horizontal direction [70]. The model describes a 2D TSCs with opposite Chern numbers within class D. This system hosts a pair of counterpropagating Majorana edge modes along its boundary. The presence of reflection symmetry in the system prevents these edge modes from gapping out. To achieve a higher-order topological phase, we introduce an additional mass term. This term effectively gaps the 1D lower boundary modes of conventional topological phases. As a result, Dirac-mass domain wall states emerge at the intersections between adjacent boundaries.

---

[1] W. A. Benalcazar, B. A. Bernevig, and T. L. Hughes, Quantized electric multipole insulators, Science **357**, 61 (2017).

[2] W. A. Benalcazar, B. A. Bernevig, and T. L. Hughes, Electric multipole moments, topological multipole moment pumping, and chiral hinge states in crystalline insulators, Phys. Rev. B **96**, 245115 (2017).

[3] F. Schindler, A. M. Cook, M. G. Vergniory, Z. Wang, S. S. P. Parkin, B. A. Bernevig, and T. Neupert, Higher-order topological insulators, Sci. Adv. **4**, eaat0346 (2018).

[4] Z. Song, Z. Fang, and C. Fang, $(d-2)$-dimensional edge states of rotation symmetry protected topological states, Phys. Rev. Lett. **119**, 246402 (2017).

[5] F. Schindler, Z. Wang, M. G. Vergniory, A. M. Cook, A. Murani, S. Sengupta, A. Y. Kasumov, R. Deblock, S. Jeon, I. Drozdov, H. Bouchiat, S. Guéron, A. Yazdani, B. A. Bernevig, and T. Neupert, Higher-order topology in bismuth, Nat. Phys. **14**, 918 (2018).

[6] C. Yue, Y. Xu, Z. Song, H. Weng, Y.-M. Lu, C. Fang, and X. Dai, Symmetry-enforced chiral hinge states and surface quantum anomalous Hall effect in the magnetic axion insulator $\mathrm{Bi}_{2-x}\mathrm{Sm}_x\mathrm{Se}_3$, Nat. Phys. **15**, 577 (2019).

[7] X.-L. Sheng, C. Chen, H. Liu, Z. Chen, Z.-M. Yu, Y. X. Zhao, and S. A. Yang, Two-dimensional second-order topological insulator in graphdiyne, Phys. Rev. Lett. **123**, 256402 (2019).

[8] C. Fang and L. Fu, New classes of topological crystalline insulators having surface rotation anomaly, Sci. Adv. **5**, eaat2374 (2019).

[9] Y. Xu, Z. Song, Z. Wang, H. Weng, and X. Dai, Higher-order topology of the axion insulator $\mathrm{EuIn_2As_2}$, Phys. Rev. Lett. **122**, 256402 (2019).

[10] M. Ezawa, Higher-order topological insulators and semimetals on the breathing kagome and pyrochlore lattices, Phys. Rev. Lett. **120**, 026801 (2018).

[11] M. Ezawa, Topological switch between second-order topological insulators and topological crystalline insulators, Phys. Rev. Lett. **121**, 116801 (2018).

[12] M. Ezawa, Magnetic second-order topological insulators and semimetals, Phys. Rev. B **97**, 155305 (2018).

[13] M. Ezawa, Strong and weak second-order topological insulators with hexagonal symmetry and $\mathbb{Z}_3$ index, Phys. Rev. B **97**, 241402(R) (2018).

[14] F. K. Kunst, G. van Miert, and E. J. Bergholtz, Lattice models with exactly solvable topological hinge and corner states, Phys. Rev. B **97**, 241405(R) (2018).

[15] M. Ezawa, Minimal models for Wannier-type higher-order topological insulators and phosphorene, Phys. Rev. B **98**, 045125 (2018).

[16] G. van Miert and C. Ortix, Higher-order topological insulators protected by inversion and rotoinversion symmetries, Phys. Rev. B **98**, 081110(R) (2018).

[17] S. Franca, J. van den Brink, and I. C. Fulga, An anomalous higher-order topological insulator, Phys. Rev. B **98**, 201114(R) (2018).

[18] Y. You, T. Devakul, F. J. Burnell, and T. Neupert, Higher-order symmetry-protected topological states for interacting bosons and fermions, Phys. Rev. B **98**, 235102 (2018).

[19] M. Lin and T. L. Hughes, Topological quadrupolar semimetals, Phys. Rev. B **98**, 241103(R) (2018).

[20] L. Trifunovic and P. W. Brouwer, Higher-order bulk-boundary correspondence for topological crystalline phases, Phys. Rev. X **9**, 011012 (2019).

[21] J. Ahn, S. Park, and B.-J. Yang, Failure of Nielsen-Ninomiya theorem and fragile topology in two-dimensional systems with space-time inversion symmetry: Application to twisted bilayer graphene at magic angle, Phys. Rev. X **9**, 021013 (2019).

[22] C. H. Lee, L. Li, and J. Gong, Hybrid higher-order skin-topological modes in nonreciprocal systems, Phys. Rev. Lett. **123**, 016805 (2019).

[23] T. Liu, Y.-R. Zhang, Q. Ai, Z. Gong, K. Kawabata, M. Ueda, and F. Nori, Second-order topological phases in non-Hermitian systems, Phys. Rev. Lett. **122**, 076801 (2019).

[24] F. Liu, H.-Y. Deng, and K. Wakabayashi, Helical topological edge states in a quadrupole phase, Phys. Rev. Lett. **122**, 086804 (2019).

[25] Z. Wang, B. J. Wieder, J. Li, B. Yan, and B. A. Bernevig, Higher-order topology, monopole nodal lines, and the origin of large fermi arcs in transition metal dichalcogenides $X\text{Te}_2$ ($X = \text{Mo, W}$), Phys. Rev. Lett. **123**, 186401 (2019).

[26] D. Călugăru, V. Juričić, and B. Roy, Higher-order topological phases: A general principle of construction, Phys. Rev. B **99**, 041301(R) (2019).

[27] W. A. Benalcazar, T. Li, and T. L. Hughes, Quantization of fractional corner charge in C_n-symmetric higher-order topological crystalline insulators, Phys. Rev. B **99**, 245151 (2019).

[28] Y. Hwang, J. Ahn, and B.-J. Yang, Fragile topology protected by inversion symmetry: Diagnosis, bulk-boundary correspondence, and Wilson loop, Phys. Rev. B **100**, 205126 (2019).

[29] R. Okugawa, S. Hayashi, and T. Nakanishi, Second-order topological phases protected by chiral symmetry, Phys. Rev. B **100**, 235302 (2019).

[30] M. Serra-Garcia, V. Peri, R. Süsstrunk, O. R. Bilal, T. Larsen, L. G. Villanueva, and S. D. Huber, Observation of a phononic quadrupole topological insulator, Nature (London) **555**, 342 (2018).

[31] C. W. Peterson, W. A. Benalcazar, T. L. Hughes, and G. Bahl, A quantized microwave quadrupole insulator with topologically protected corner states, Nature (London) **555**, 346 (2018).

[32] H. Xue, Y. Yang, F. Gao, Y. Chong, and B. Zhang, Acoustic higher-order topological insulator on a Kagome lattice, Nat. Mater. **18**, 108 (2019).

[33] X. Ni, M. Weiner, A. Alu, and A. B. Khanikaev, Observation of higher-order topological acoustic states protected by generalized chiral symmetry, Nat. Mater. **18**, 113 (2019).

[34] J. Noh, W. A. Benalcazar, S. Huang, M. J. Collins, K. P. Chen, T. L. Hughes, and M. C. Rechtsman, Topological protection of photonic mid-gap defect modes, Nat. Photonics **12**, 408 (2018).

[35] S. Imhof, C. Berger, F. Bayer, J. Brehm, L. W. Molenkamp, T. Kiessling, F. Schindler, C. H. Lee, M. Greiter, T. Neupert, and R. Thomale, Topolectrical-circuit realization of topological corner modes, Nat. Phys. **14**, 925 (2018).

[36] X. Zhang, H.-X. Wang, Z.-K. Lin, Y. Tian, B. Xie, M.-H. Lu, Y.-F. Chen, and J.-H. Jiang, Second-order topology and multidimensional topological transitions in sonic crystals, Nat. Phys. **15**, 582 (2019).

[37] S. N. Kempkes, M. R. Slot, J. J. van Den Broeke, P. Capiod, W. A. Benalcazar, D. Vanmaekelbergh, D. Bercioux, I. Swart, and C. M. Smith, Robust zero-energy modes in an electronic higher-order topological insulator, Nat. Mater. **18**, 1292 (2019).

[38] S. Mittal, V. V. Orre, G. Zhu, M. A. Gorlach, A. Poddubny, and M. Hafezi, Photonic quadrupole topological phases, Nat. Photonics **13**, 692 (2019).

[39] R.-X. Zhang, F. Wu, and S. Das Sarma, Möbius insulator and higher-order topology in $\text{MnBi}_{2n}\text{Te}_{3n+1}$, Phys. Rev. Lett. **124**, 136407 (2020).

[40] E. Lee, R. Kim, J. Ahn, and B.-J. Yang, Two-dimensional higher-order topology in monolayer graphdiyne, npj Quantum Mater. **5**, 1 (2020).

[41] Y. Ren, Z. Qiao, and Q. Niu, Engineering corner states from two-dimensional topological insulators, Phys. Rev. Lett. **124**, 166804 (2020).

[42] C. Chen, Z. Song, J.-Z. Zhao, Z. Chen, Z.-M. Yu, X.-L. Sheng, and S. A. Yang, Universal approach to magnetic second-order topological insulator, Phys. Rev. Lett. **125**, 056402 (2020).

[43] B. Liu, L. Xian, H. Mu, G. Zhao, Z. Liu, A. Rubio, and Z. F. Wang, Higher-order band topology in twisted moiré superlattice, Phys. Rev. Lett. **126**, 066401 (2021).

[44] H. Huang and F. Liu, Higher-order topology induced by structural buckling, Natl. Sci. Rev. **9**, nwab170 (2022).

[45] M. Pan, D. Li, J. Fan, and H. Huang, Two-dimensional Stiefel-Whitney insulators in liganded Xenes, npj Comput. Mater. **8**, 1 (2022).

[46] H. Mu, G. Zhao, H. Zhang, and Z. Wang, Antiferromagnetic second-order topological insulator with fractional mass-kink, npj Comput. Mater. **8**, 82 (2022).

[47] W. A. Benalcazar, J. C. Y. Teo, and T. L. Hughes, Classification of two-dimensional topological crystalline superconductors and Majorana bound states at disclinations, Phys. Rev. B **89**, 224503 (2014).

[48] J. Langbehn, Y. Peng, L. Trifunovic, F. von Oppen, and P. W. Brouwer, Reflection-symmetric second-order topological insulators and superconductors, Phys. Rev. Lett. **119**, 246401 (2017).

[49] M. Geier, L. Trifunovic, M. Hoskam, and P. W. Brouwer, Second-order topological insulators and superconductors with an order-two crystalline symmetry, Phys. Rev. B **97**, 205135 (2018).

[50] E. Khalaf, Higher-order topological insulators and superconductors protected by inversion symmetry, Phys. Rev. B **97**, 205136 (2018).

[51] Z. Yan, F. Song, and Z. Wang, Majorana corner modes in a high-temperature platform, Phys. Rev. Lett. **121**, 096803 (2018).

[52] Q. Wang, C.-C. Liu, Y.-M. Lu, and F. Zhang, High-temperature Majorana corner states, Phys. Rev. Lett. **121**, 186801 (2018).

[53] H. Shapourian, Y. Wang, and S. Ryu, Topological crystalline superconductivity and second-order topological superconductivity in nodal-loop materials, Phys. Rev. B **97**, 094508 (2018).

[54] V. Dwivedi, C. Hickey, T. Eschmann, and S. Trebst, Majorana corner modes in a second-order Kitaev spin liquid, Phys. Rev. B **98**, 054432 (2018).

[55] Y. Wang, M. Lin, and T. L. Hughes, Weak-pairing higher order topological superconductors, Phys. Rev. B **98**, 165144 (2018).

[56] T. Liu, J. J. He, and F. Nori, Majorana corner states in a two-dimensional magnetic topological insulator on a high-temperature superconductor, Phys. Rev. B **98**, 245413 (2018).

[57] X.-H. Pan, K.-J. Yang, L. Chen, G. Xu, C.-X. Liu, and X. Liu, Lattice-symmetry-assisted second-order topological superconductors and Majorana patterns, Phys. Rev. Lett. **123**, 156801 (2019).

[58] Z. Yan, Higher-order topological odd-parity superconductors, Phys. Rev. Lett. **123**, 177001 (2019).

[59] X. Zhu, Second-order topological superconductors with mixed pairing, Phys. Rev. Lett. **122**, 236401 (2019).

[60] N. Bultinck, B. A. Bernevig, and M. P. Zaletel, Three-dimensional superconductors with hybrid higher-order topology, Phys. Rev. B **99**, 125149 (2019).

[61] Z. Yan, Majorana corner and hinge modes in second-order topological insulator/superconductor heterostructures, Phys. Rev. B **100**, 205406 (2019).

[62] C.-H. Hsu, P. Stano, J. Klinovaja, and D. Loss, Majorana Kramers pairs in higher-order topological insulators, Phys. Rev. Lett. **121**, 196801 (2018).

[63] Y. Volpez, D. Loss, and J. Klinovaja, Second-order topological superconductivity in π-junction Rashba layers, Phys. Rev. Lett. **122**, 126402 (2019).

[64] S. Franca, D. V. Efremov, and I. C. Fulga, Phase-tunable second-order topological superconductor, Phys. Rev. B **100**, 075415 (2019).

[65] Y.-T. Hsu, W. S. Cole, R.-X. Zhang, and J. D. Sau, Inversion-protected higher-order topological superconductivity in monolayer WTe_2, Phys. Rev. Lett. **125**, 097001 (2020).

[66] R.-X. Zhang, Y.-T. Hsu, and S. Das Sarma, Higher-order topological Dirac superconductors, Phys. Rev. B **102**, 094503 (2020).

[67] L. Fu, Topological crystalline insulators, Phys. Rev. Lett. **106**, 106802 (2011).

[68] Y. Ando and L. Fu, Topological crystalline insulators and topological superconductors: From concepts to materials, Annu. Rev. Condens. Matter Phys. **6**, 361 (2015).

[69] D. Varjas, A. Lau, K. Pöyhönen, A. R. Akhmerov, D. I. Pikulin, and I. C. Fulga, Topological phases without crystalline counterparts, Phys. Rev. Lett. **123**, 196401 (2019).

[70] R. Chen, C.-Z. Chen, J.-H. Gao, B. Zhou, and D.-H. Xu, Higher-order topological insulators in quasicrystals, Phys. Rev. Lett. **124**, 036803 (2020).

[71] C.-B. Hua, R. Chen, B. Zhou, and D.-H. Xu, Higher-order topological insulator in a dodecagonal quasicrystal, Phys. Rev. B **102**, 241102(R) (2020).

[72] A. Agarwala, V. Juričić, and B. Roy, Higher-order topological insulators in amorphous solids, Phys. Rev. Res. **2**, 012067(R) (2020).

[73] S. Spurrier and N. R. Cooper, Kane-Mele with a twist: Quasicrystalline higher-order topological insulators with fractional mass kinks, Phys. Rev. Res. **2**, 033071 (2020).

[74] B. Lv, R. Chen, R. Li, C. Guan, B. Zhou, G. Dong, C. Zhao, Y. Li, Y. Wang, H. Tao, J. Shi, and D.-H. Xu, Realization of quasicrystalline quadrupole topological insulators in electrical circuits, Commun. Phys. **4**, 108 (2021).

[75] T. Peng, C.-B. Hua, R. Chen, Z.-R. Liu, D.-H. Xu, and B. Zhou, Higher-order topological Anderson insulators in quasicrystals, Phys. Rev. B **104**, 245302 (2021).

[76] H. Huang, J. Fan, D. Li, and F. Liu, Generic orbital design of higher-order topological quasicrystalline insulators with odd five-fold rotation symmetry, Nano Lett. **21**, 7056 (2021).

[77] J. Fan and H. Huang, Topological states in quasicrystals, Front. Phys. **17**, 13203 (2022).

[78] L. Xiong, Y. Zhang, Y. Liu, Y. Zheng, and X. Jiang, Higher-order topological states in photonic Thue-Morse quasicrystals: Quadrupole insulator and the origin of corner states, Phys. Rev. Appl. **18**, 064089 (2022).

[79] C. Wang, F. Liu, and H. Huang, Effective model for fractional topological corner modes in quasicrystals, Phys. Rev. Lett. **129**, 056403 (2022).

[80] A. Shi, Y. Peng, J. Jiang, Y. Peng, P. Peng, J. Chen, H. Chen, S. Wen, X. Lin, F. Gao, and J. Liu, Observation of topological corner state arrays in photonic quasicrystals, Laser Photonics Rev. 2300956 (2024).

[81] Y.-L. Tao, J.-H. Wang, and Y. Xu, Average symmetry protected higher-order topological amorphous insulators, SciPost Phys. **15**, 193 (2023).

[82] C. Rangi, K.-M. Tam, and J. Moreno, Engineering a non-Hermitian second-order topological insulator state in quasicrystals, Phys. Rev. B **109**, 064203 (2024).

[83] Y.-F. Mao, Y.-L. Tao, J.-H. Wang, Q.-B. Zeng, and Y. Xu, Higher-order topological insulators and semimetals in three dimensions without crystalline counterparts, arXiv:2307.14974.

[87] T. Dotera, S. Bekku, and P. Ziherl, Bronze-mean hexagonal quasicrystal, Nat. Mater. **16**, 987 (2017).

[88] See Supplemental Material at http://link.aps.org/supplemental/10.1103/PhysRevB.109.L121403 for more detailed discussions, including the tiling construction of bronze-mean hexagonal quasicrystal; the results of other Wilson mass terms and symmetry analysis in sixfold symmetric quasicrystal; the robustness of Majorana zero-energy modes within the quasicrystalline second-order topological superconductor; the extension of these findings for other rotationally symmetric quasicrystalline systems; the generalization of three-dimensional higher-order topological semimetal in sixfold symmetric quasicrystals, which also includes Refs. [66,84,86,87,99–101].

[89] I. C. Fulga, D. I. Pikulin, and T. A. Loring, Aperiodic weak topological superconductors, Phys. Rev. Lett. **116**, 257002 (2016).

[90] N. Read and D. Green, Paired states of fermions in two dimensions with breaking of parity and time-reversal symmetries and the fractional quantum Hall effect, Phys. Rev. B **61**, 10267 (2000).

[84] A. R. Buitrago, Polygons, diagonals, and the bronze mean, Nexus Netw. J. **9**, 321 (2007).

[85] A. L. Mackay, Crystallography and the Penrose pattern, Physica A **114**, 609 (1982).

[86] B. Grünbaum and G. C. Shephard, *Tilings and Patterns* (W. H. Freeman & Co., USA, 1986).

[91] R. Jackiw and C. Rebbi, Solitons with fermion number 1/2, Phys. Rev. D **13**, 3398 (1976).

[92] H. Spring, A. R. Akhmerov, and D. Varjas, Amorphous topological phases protected by continuous rotation symmetry, SciPost Phys. **11**, 022 (2021).

[93] R. Chen, B. Zhou, and D.-H. Xu, Quasicrystalline second-order topological semimetals, Phys. Rev. B **108**, 195306 (2023).

[94] G. Pelegrí, A. M. Marques, V. Ahufinger, J. Mompart, and R. G. Dias, Second-order topological corner states with ultracold atoms carrying orbital angular momentum in optical lattices, Phys. Rev. B **100**, 205109 (2019).

[95] D. Asahi and N. Nagaosa, Topological indices, defects, and Majorana fermions in chiral superconductors, Phys. Rev. B **86**, 100504(R) (2012).

[96] I. Seroussi, E. Berg, and Y. Oreg, Topological superconducting phases of weakly coupled quantum wires, Phys. Rev. B **89**, 104523 (2014).

[97] A. Bühler, N. Lang, C. V. Kraus, G. Möller, S. D. Huber, and H.-P. Büchler, Majorana modes and *p*-wave superfluids for fermionic atoms in optical lattices, Nat. Commun. **5**, 4504 (2014).

[98] M. Diez, I. C. Fulga, D. I. Pikulin, J. Tworzydło, and C. W. J. Beenakker, Bimodal conductance distribution of Kitaev edge modes in topological superconductors, New J. Phys. **16**, 063049 (2014).

[99] J. Millar, Filling-the-gaps method to generate a symmetric substitution tiling for any n with inflation factor < 2, https://patternblockhead.com.

[100] A. Madison, Constructing Penrose-like tilings with 7-fold symmetry, Struct. Chem. **29**, 645 (2018).

[101] P. Stampfli, A dodecagonal quasiperiodic lattice in two dimensions, Helv. Phys. Acta **59**, 1260 (1986).